Soft Matter

PAPER

View Article Online
View Journal | View Issue

Cite this: *Soft Matter*, 2023, **19**, 3551

Flows of a nonequilibrated aqueous two-phase system in a microchannel†

Niki Abbasi, [a] Janine K. Nunes, [a] Zehao Pan, [a] Tejas Dethe, [a] Ho Cheung Shum, [b] Andrej Košmrlj [ac] and Howard A. Stone *[a]

Received 22nd February 2023,
Accepted 24th April 2023

DOI: 10.1039/d3sm00233k

rsc.li/soft-matter-journal

Liquid–liquid phase separation is a rich and dynamic process, which recently has gained new interest, especially in biology and for material synthesis. In this work, we experimentally show that co-flow of a nonequilibrated aqueous two-phase system within a planar flow-focusing microfluidic device results in a three-dimensional flow, as the two nonequilibrated solutions move downstream along the length of the microchannel. After the system reaches steady-state, invasion fronts from the outer stream are formed along the top and bottom walls of the microfluidic device. The invasion fronts advance towards the center of the channel, until they merge. We first show by tuning the concentration of polymer species within the system that the formation of these fronts is due to liquid–liquid phase separation. Moreover, the rate of invasion from the outer stream increases with increasing polymer concentrations in the streams. We hypothesize the invasion front formation and growth is driven by Marangoni flow induced by the polymer concentration gradient along the width of the channel, as the system is undergoing phase separation. In addition, we show how at various downstream positions the system reaches its steady-state configuration once the two fluid streams flow side-by-side in the channel.

1 Introduction

With the advent of microfabrication,[1] both miscible and immiscible multiphase microscale flows have been studied extensively. Considering immiscible multiphase flows, the flow evolution within microchannels can result in various configurations, such as microdroplets, fluid threads, and wetting films. In contrast, systems involving chemically nonequilibrated multiphase flows, which can exhibit features of either miscible flows or dynamically transition between miscible and immiscible flow behavior, have not been well studied.

One such system is a nonequilibrated aqueous two-phase system (ATPS), which is comprised of two aqueous solutions, either polymer–polymer solutions, polymer–salt solutions, or alcohol–salt solutions, which de-mix above a certain concentration threshold that is dependent on species concentrations, molecular weight, and the interactions between the species. Traditionally used as a separation platform based on the affinity partitioning of species within each phase,[2–4] equilibrated aqueous two-phase systems have gained significant interest in the field of microfluidics due to their intrinsic biocompatible nature,[5,6] mainly for microdroplet formation[7–10] for various biotechnological applications, including, but not limited to, cell encapsulation[11] and formation of synthetic cells.[12,13] One inherent characteristic of an ATPS is its low interfacial tension, which has been reported to be as low as $\mathcal{O}(0.01)$ mN m^{-1}.[14,15]

These systems, when out of equilibrium, exhibit dynamics that is driven primarily by the transfer of the solvent from one phase to another. This process can either lead to nucleation and formation of droplets[16,17] and interfacial instabilities[18,19] while the system is undergoing liquid–liquid phase separation, or, if a higher solvent concentration is added, the system can become fully miscible.[20] Similar observations can be seen in ternary systems, where solvent extraction *via* either evaporation,[21–23] introduction of an immiscibility front[24] within a channel or bulk submersion of ternary mixtures within a solvent-poor bath,[25] result in liquid–liquid phase separation. Similarly, ternary systems within a co-flow of emulsions[26] and fluid threads[27,28] in a solvent-poor fluid, which result in formation of hierarchical structures, have been studied.

In systems undergoing liquid–liquid phase separation, a variety of different flows can evolve. These flows are not only set by the interaction between the different species and the gradient in composition, but also can be influenced strongly by the presence of solid surfaces and the wettability of each phase to the surface. For example, nucleated droplets may experience

[a] *Department of Mechanical and Aerospace Engineering, Princeton University, Princeton, NJ, USA. E-mail: hastone@princeton.edu*
[b] *Department of Mechanical Engineering, University of Hong Kong, Hong Kong, China*
[c] *Princeton Materials Institute, Princeton University, Princeton, NJ, USA*

† Electronic supplementary information (ESI) available. See DOI: https://doi.org/10.1039/d3sm00233k

unidirectional propulsion due to Marangoni flow[27,29,30] set by a gradient in composition. Colloidal particles present in a phase separating mixture may experience phoretic motion, as the composition near the particle surface changes.[31] Moreover, strong wettability of the nucleated phase to a surface can induce active spreading of a fluid front as the system undergoes phase separation.[32,33] However, the details of the flow accompanying liquid–liquid phase separation, in the presence of a background flow, has not been well-explored.

In this paper, we study how nonequilibrated aqueous two-phase systems, within a co-flow setup, evolve as they flow downstream within a microchannel. We use a nonequilibrated ATPS of dextran (DEX) and poly(ethylene glycol) (PEG). Within the flow-focusing device, we flow a miscible solution of DEX and PEG as the outer stream (labelled solution 1) surrounding an inner stream of highly concentrated DEX (labelled solution 2). In Section 3.1, we study, using confocal microscopy, the steady-state evolution of the three-dimensional flow in systems undergoing liquid–liquid phase separation. By tuning the concentration of the polymers within the system, we find that invasion fronts, which advance inwards transverse to the imposed flow direction, are formed only when the system undergoes liquid–liquid phase separation. Within the immiscible regime, tuning the concentration of the polymers present affects the downstream evolution of the three-dimensional flow, for which we provide an explanation. In Section 3.2, we experimentally show how the system reaches its steady-state configuration at different positions along the length of the channel.

2 Experimental methods

2.1 Preparation of aqueous solutions

The ATPS used consists of DEX with average molecular weight 150 000 Da (dextran from the bacterium *Leuconostoc mesenteroides*, Sigma-Alrich, St. Louis, MO, USA) and PEG (poly(ethylene glycol), BioUltra, Sigma-Alrich, St. Louis, MO, USA) with average molecular weight of 35 000 Da. The outer stream, consisting of a miscible mixture of DEX 5 w/v% and varying PEG concentration (C_{PEG_1} = 0 w/v%, 0.5 w/v%, 0.75 w/v%, 1 w/v%), and the inner stream, consisting of an aqueous solution of varying DEX concentration (C_{DEX_2} = 5 w/v%, 10 w/v%, 20 w/v%, 30 w/v%), are prepared in de-ionized (DI) water. After mixing the polymer solutions using a vortex mixer, the solutions are sonicated for approximately one hour until the polymer fully dissolves in DI water. The viscosities of the solutions are measured using a rheometer (Anton Paar MCR 302e).

The outer stream is doped with Alexa Fluor dye (Alexa Fluor TM 633 C5-maleimide, Invitrogen by Thermo Fisher Scientific, Waltham, MA, USA). To dope the outer stream with this dye, first a stock solution is formed by making a 10 mM dye solution in dimethyl sulfoxide (DMSO). Then, 1 μl ml^{-1} of the dye stock solution is added to the miscible outer stream of DEX and PEG. This dye was chosen to dope the outer stream, since Alexa Fluor has been shown to have an affinity to the PEG phase,[34] which makes it a suitable tracer for PEG.

2.2 Device fabrication

Standard soft lithography methods are used to fabricate the microfluidic devices.[1] The channel design, which is comprised of two inlets and one outlet, is first drawn on AutoCAD (AutoCAD 2018, Autodesk, Inc., San Rafael, CA, USA). To make the microfluidic channel mold, SU8 2025 (Microchem, Newton, MA, USA) is spin-coated on a 4″ silicon wafer (NOVA Electronic Materials, Flower Mound, TX, USA). Then, the channel design is exposed onto the wafer substrate using a direct-write system (Heidelberg PG 101, Heidelberg Instruments, Heidelberg, Germany). The patterns are then developed by immersing the wafer in a developer solution (Microchem, Newton, MA, USA). Once the patterns are fully developed, the wafer is dried and placed inside a Petri dish, forming the mold of the microfluidic device.

After preparation of the mold, polydimethylsiloxane (PDMS, Sylgard TM 184 Silicone elastomer kit, Ellsworth Adhesives, Germantown, WI, USA), with ratio of 10 : 1 of polymeric base to curing agent, is used to fill the mold. The substrate of the device is prepared by spin coating a thin layer of PDMS mixture (at a speed of 2000 RPM for 30 s) on a plain microscope slide (25 × 75 × 1 mm, Fisher Scientific, Waltham, MA, USA). The mold and the PDMS-coated substrates are kept inside a 65 °C oven for approximately 3 hours. Once cured, PDMS chips are cut out from the mold and plasma treated using a laboratory corona treater (Model BD-20AC, Electro-Technic Products Inc., Chicago, IL, USA). After the treatment, the substrate and the PDMS chip are bonded together and kept inside a 65 °C oven for 12 hours to render the device walls hydrophobic relative to right after plasma treatment.[35] For each experiment new devices are prepared, with plasma treatment and time in the oven maintained the same to ensure uniform surface properties across all devices.

2.3 Experimental setup

Syringe pumps (Harvard Apparatus, Holliston, MA, USA) are used to flow the solutions into the microfluidic device. First, the device is filled with the outer stream fluid at a constant flow rate of 2 μl min^{-1}. Once all channels of the device are filled, then the inner stream is injected into the microfluidic device at a constant flow rate of 1 μl min^{-1}. In all experiments, the flow rates of the outer and inner streams are Q_1 = 2 μl min^{-1} and Q_2 = 1 μl min^{-1}, respectively. The microfluidic device setup is illustrated in Fig. 1(a) and (b). Based on the given flow rates, the average axial velocities of solutions 1 and 2 are calculated to be $U_1 = \mathcal{O}(10^{-3})$ m s^{-1} and $U_2 = \mathcal{O}(10^{-4})$ m s^{-1}. To characterize the flow system and compare the axial advection downstream along the length of the channel with transverse diffusion, the Peclet number for each stream is calculated where $\mathrm{Pe} = \left(\frac{w_{\mathrm{ch}}}{2}\right)^2 U/LD$. Considering the diffusivity of water, which is the fastest diffusing species in the system and the flow velocity along z direction, is $\mathrm{Pe}_1 = \mathcal{O}(1)$ and $\mathrm{Pe}_2 = \mathcal{O}(10^{-1})$, with w_{ch} = 600 μm, L = 22 mm and $D \approx 10^{-9}$ m^2 s^{-1} is the typical diffusion coefficient. Based on the estimate of $\mathrm{Pe}_1 = \mathcal{O}(1)$, and considering solely advection

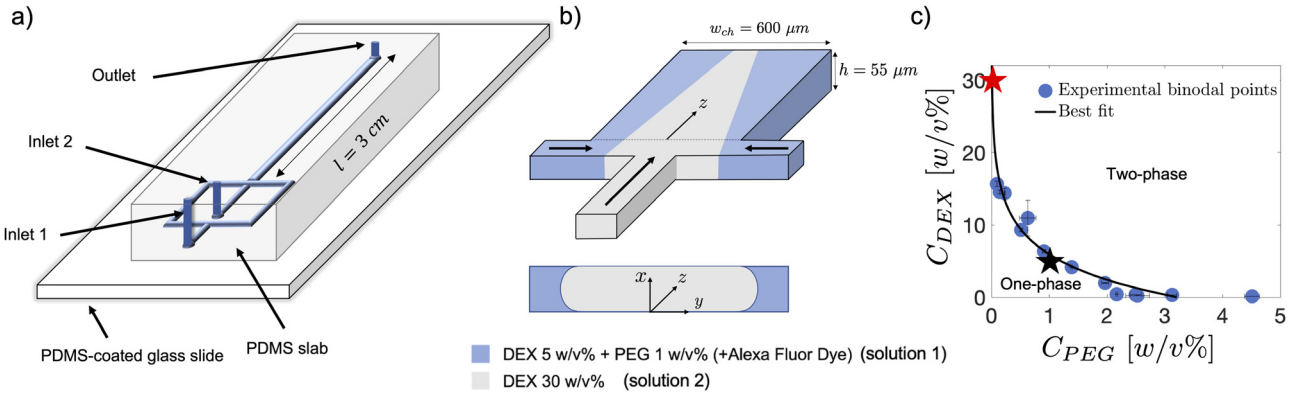

Fig. 1 (a) Schematic of the microfluidic device used for this study. A flow-focusing all-PDMS microfluidic device is used to flow two nonequilibrated polymer solutions side by side. (b) A miscible mixture of DEX 5 w/v% and PEG 1 w/v% is flowed as the outer stream, and a highly concentrated DEX 30 w/v% is flowed as the inner stream. Alexa Fluor TM 633 C5-maleimide is added to the outer stream for visualization purposes. (c) Experimentally generated binodal curve of ATPS of DEX 150 000 Da and PEG 35 000 Da, where the vertical and horizontal axes are the concentration of DEX, C_{DEX}, and concentration of PEG, C_{PEG}, respectively (see Section S1, ESI† for more information about the binodal curve and exponential fitting through the binodal points.) The blue circles indicate the points on the binodal curve. The composition of the outer (solution 1) and inner (solution 2) streams, which are both within the miscible one-phase region, are highlighted with black and red stars, respectively.

downstream in the z direction and diffusion of water in the y direction, water can diffuse from the outer stream towards the centerline of the channel as it moves along the whole length of the channel.

A confocal microscope (Leica SP5, Leica, Wetzlar, Germany) is used to image the three-dimensional flow within the microchannel by visualizing the Alexa dye present within the outer stream, using a 633 nm laser at 110 W laser power. For steady-state imaging, we wait approximately 30 minutes from the time the inner stream is injected into the channel before we start imaging, which we have verified is long enough for the system to reach steady-state. We obtain cross-sectional views of the microchannel by scanning across the channel height at a frequency of 400 Hz, at different positions downstream along the length of the device. For the unsteady temporal experiments, we perform scanning using a resonant scanner, which allows for scanning at a frequency of 8000 Hz. We use MATLAB (MathWorks, Natick, MA, USA) and FIJI software[36] to analyze and perform image processing.

3 Results and discussion

3.1 System at steady-state

First, we will describe how a system consisting of a miscible outer stream of DEX 5 w/v% and PEG 1 w/v% (solution 1), and an inner stream of DEX 30 w/v% (solution 2) evolves inside the microchannel. The compositions of these two solutions are indicated on the phase diagram, as shown in Fig. 1(c) with star markers. After approximately 30 minutes from the time solution 2 is injected into the device, the flow system reaches a steady-state, *i.e.*, there are no changes in time at each cross section of the channel. Fluorescent images of the junction of the device in the y–z plane, close to either the top or bottom wall (similar to the image in Fig. 2(a)), show fronts that move towards the center of the channel. It is evident from cross-sectional x–y views of the microchannel that invasion fronts are formed from the outer stream, towards the inner stream, on both the top and bottom walls of the device, as shown in Fig. 2(b) and Video 1, ESI.† Imaging along the length of the channel, we observe that these fronts grow and at $z \approx 5$ mm downstream, they merge. Furthermore, it can be seen that the Alexa Fluor dye intensity at the tip of the fronts increases along the downstream direction.

At early times, as sketched in Fig. 2(c), we expect that a chemical gradient between the two streams is such that water will be withdrawn from the outer stream towards the inner stream. The withdrawal is expected to be more pronounced near the walls, since advection will be less dominant due to the no-slip condition. This in turn would increase the concentration of the PEG and DEX species in the outer stream. If the PEG and DEX concentrations increase above the binodal curve, a PEG-rich phase will nucleate (PEG is the species with the lowest volume fraction), which we observe experimentally with the appearance of PEG-rich zones on the top and bottom walls of the microchannel (Fig. 2(b)). The heterogeneous nucleation of PEG on the wall is favourable, since the walls of the device are hydrophobic, and the phase-separated PEG is more hydrophobic compared to the DEX phase.[37]

Besides the PEG front that nucleates and moves on the top and bottom walls, PEG droplets can be seen near the diffuse interface of the inner and outer streams (see Fig. S2 in Section S2, ESI†). These droplets grow, coarsen and coalesce as they flow downstream with an initially diagonal trajectory relative to channel side walls (parallel to the tips of the nucleated PEG-rich front). Some evidence of these PEG droplets can be seen in the cross sectional view of the channel in Fig. 2(b).

It is known from the literature of aqueous two-phase systems that the interfacial tension is directly correlated with the

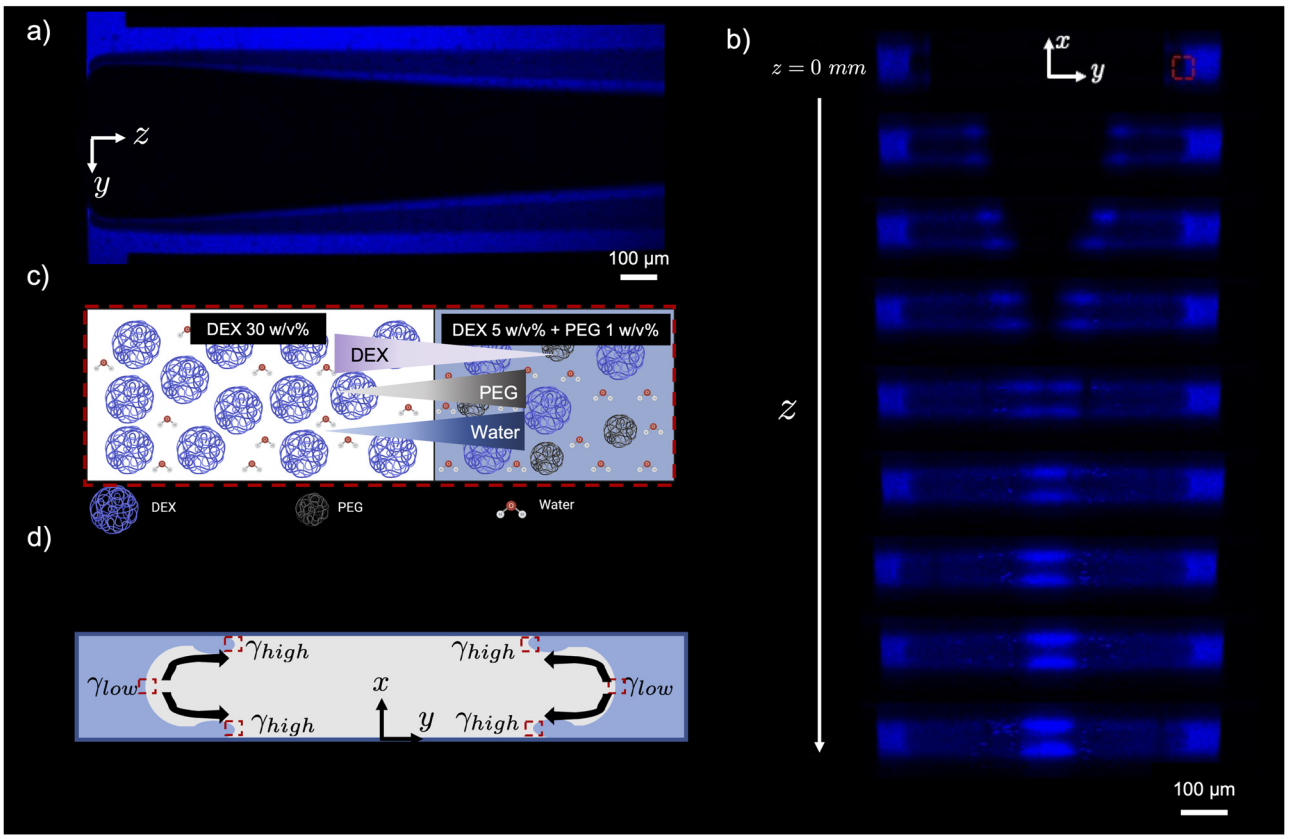

Fig. 2 (a) Fluorescent image of the y–z view of the flow-focusing junction of the microchannel at $x \approx 0$ (the bottom of the channel), after the system reaches steady-state, where the inner stream of DEX 30 w/v% (not visualized) is surrounded by a miscible solution of DEX 5 w/v% and PEG 1 w/v% (doped with Alexa Fluor dye). Two fronts can be seen moving towards the center of the channel. (b) Steady-state confocal microscopy images showing flow cross sections every 1 mm downstream along the z direction. Upstream, moving fronts from the outer streams are formed on both top and bottom walls of the device. The fronts move towards the center of the channel further along z, and at about $z \approx 5$ mm they merge, resulting in formation of a central fluid thread on the top and bottom walls. (c) Illustration of species within the system at early times within the red rectangle shown in (b), near the diffuse boundary between solutions 1 and 2. The image is created with (**https://www.biorender.com**). The concentrations of species are set such that water will be withdrawn from the outer towards the inner stream, and should be faster near the walls due to weaker effects of convection (no-slip condition). This schematic indicates the relative concentration of species across the two fluid streams, and does not provide any insight on the conformation and polymer chain morphology in the solution. (d) Schematic of the channel cross section illustrating the proposed mechanism for the advancement of the fronts. The withdrawal of water from the outer stream towards the inner stream near the walls results in an increase of polymer concentrations and therefore induces phase separation and nucleation of a PEG-rich zone near the interface. Due to the concentration gradient present across the interface between the two streams, a gradient in tension $\nabla\gamma$ induces Marangoni flow, causing the PEG-rich zone to move towards the center of the channel, forming fronts on both top and bottom walls, with the original nucleated PEG-rich zone being the tip of these moving fronts.

concentration of polymers within ATPS.[14,38] Therefore, our observations suggest that moving along the interface between the two streams in the direction of center of the channel the interfacial tension increases. As shown in Fig. 2(d), the composition gradient along the interface effectively results in Marangoni flow from the outer stream towards the inner stream, transverse to the main flow direction, inducing advancement of these invasion fronts towards the center line of the channel, as the fluids in the different phases flow downstream along the length of the device.

3.1.1 Effect of polymer concentration on formation and advancement of PEG-nucleated fronts. Next, to test these ideas of an effective interfacial tension gradient, we tune the concentration of the polymer species within the flow system to observe whether the results are consistent with Marangoni flow. To do so, we first vary the PEG concentration (from 0, 0.5, 0.75 and 1 w/v%) in the outer stream, while keeping the DEX concentration in the inner and outer streams constant. In another set of experiments, we keep the concentration of PEG and DEX in the outer stream constant, while tuning the concentration of the DEX in the inner stream (5, 10, 20 and 30 w/v%). As the concentration of either PEG in the outer stream or the DEX in the inner stream is increased, the system becomes more susceptible to phase separation. As seen in Fig. 3(a) and Video 2 ESI,† for the cases where PEG concentration is 0 or 0.5 w/v%, no invasion fronts are formed. These cases behave like miscible co-flowing systems, where the chemical gradients drive diffusion of the different molecular species across the streams, as evidenced by the diffusion of the Alexa Fluor dye from the outer stream towards the inner stream. At PEG concentrations of 0.75 w/v% and 1 w/v%, the PEG concentration is large enough that the system undergoes liquid–liquid phase separation. Therefore PEG zones nucleate

near the interface between the outer and inner streams and the invasion fronts grow in width with increasing downstream positions. In other words, the invasion fronts grow in time, since the difference in downstream positions is proportional to the time a fluid element spends moving between the two locations. Qualitatively, we observe that the higher the PEG concentration the faster the rate of invasion.

Trends observed in experiments where the inner DEX concentration is tuned are similar to experiments where the outer stream PEG concentration is varied. For an inner stream DEX concentration of 5 and 10 w/v%, we only observe diffusion of the Alexa Fluor dye towards the inner stream and no invasion front formation, indicating that the inner and outer streams are miscible (Fig. 3(b)). However, for higher DEX concentrations of

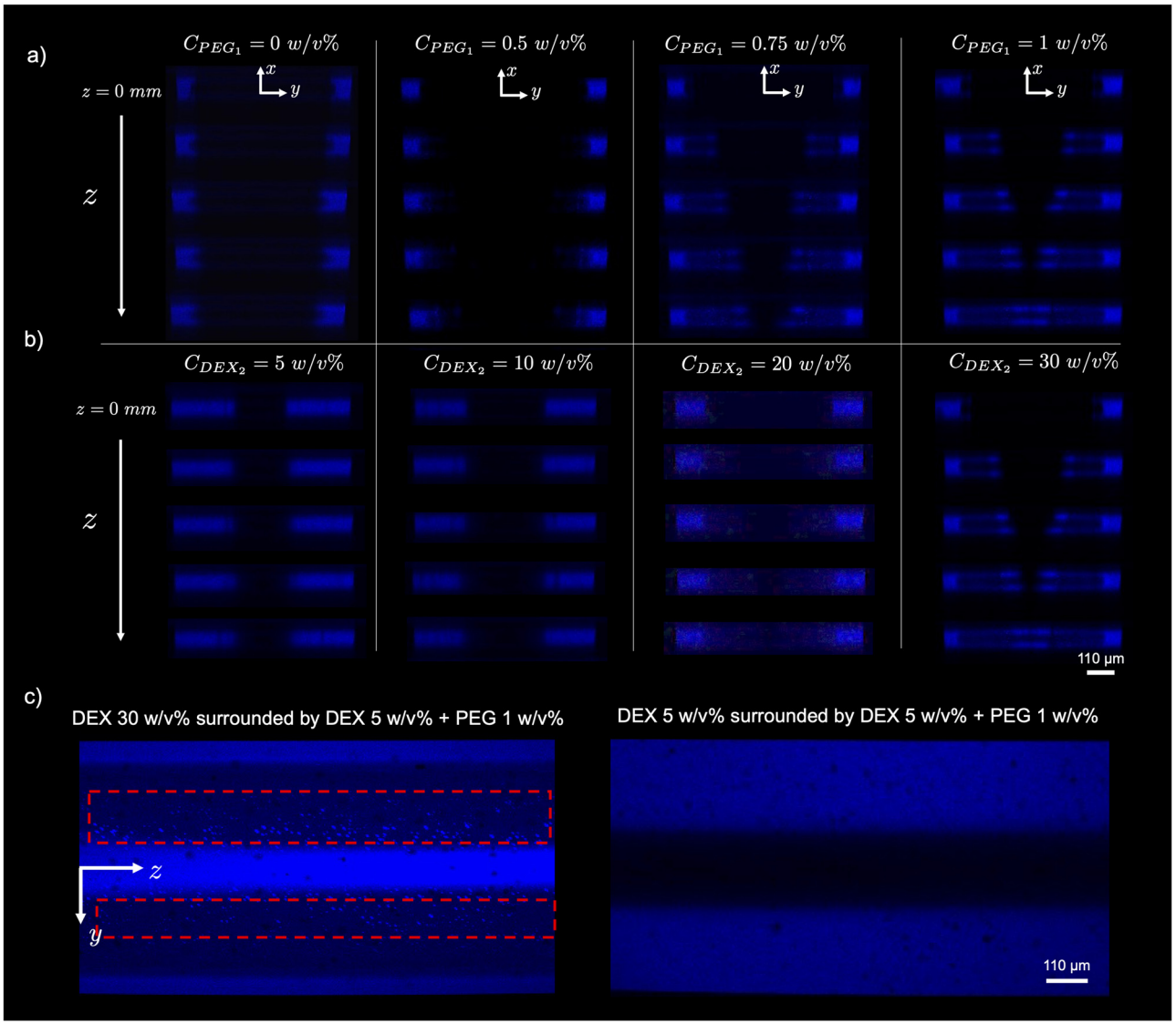

Fig. 3 Confocal microscopy scans in the x–y plane, taken every 1 mm downstream in z, for different systems where (a) C_{PEG_1} is varied from 0, 0.5, 0.75 and 1 w/v% while keeping C_{DEX_1} = 5 w/v% and C_{DEX_2} = 30 w/v% and (b) C_{DEX_2} is varied from 5, 10, 20 and 30 w/v% while keeping C_{DEX_1} = 5 w/v% and C_{PEG_1} = 1 w/v%, with all experiments set with Q_1 = 2 μl min^{-1} and Q_2 = 1 μl min^{-1}. As seen in panel a, With C_{PEG_1} of 0 and 0.5 w/v%, after the flow reaches steady-state, invasion fronts are not formed. Instead, we observe that the Alexa Fluor dye diffuses from the outer streams towards the center of the channel. With no PEG in the system or a low C_{PEG_1} = 0.5 w/v%, the initial concentration of the system is set within the miscible regime, therefore no liquid–liquid phase separation occurs. As C_{PEG_1} is increased to 0.75 and 1 w/v%, the system undergoes liquid–liquid phase separation and invasion fronts can be seen moving towards the center of the channel. Similarly, for experiments where C_{DEX_2} is tuned (as shown in panel b), lower C_{DEX_2} of 5 and 10 w/v% do not exhibit an advancing front, since the flow system is fully miscible. However, for higher concentration of C_{DEX_2} of 20 or 30 w/v%, the system becomes susceptible to liquid–liquid phase separation, therefore triggering nucleation of a PEG-rich phase near the interface and then formation of a PEG-rich moving front due to a gradient in tension present across the width of the front. (c) Fluorescent flow images in the y–z plane at $x \approx 50$ μm (at the top wall of the channel) and z ranging from 5 mm to 6.5 mm, for system of DEX 30 w/v% surrounded by miscible solution of DEX 5 w/v% and PEG 1 w/v% (left image) and DEX 5 w/v% surrounded by miscible solution of DEX 5 w/v% and PEG 1 w/v% (right image). PEG-rich droplets can be seen flowing parallel to the nucleated PEG film on the top wall (within the dashed red box in the left image), while no trace of phase separation can be seen in the system DEX 5 w/v% as the inner stream (right image).

20 and 30 w/v%, the system undergoes liquid–liquid phase separation, and invasion fronts form on the top and bottom walls and advance towards the channel center line. As seen in Fig. 3(b), the invasion fronts formed in the presence of DEX 20 w/v% in the inner stream, compared to DEX 30 w/v% in the inner stream, move slower and the intensity of the Alexa Fluor dye within the front is much lower. In systems where fast advancing fronts are formed, nucleated PEG droplets can be seen flowing in parallel to the nucleated zones on either top or bottom wall, as seen in Fig. 3(c), further confirming that for front formations, a high gradient in tension resulting from nonequilibrated two-phase system is required. On the other hand, in systems that are diffusive, no traces of microdroplets could be seen. As either the PEG concentration in the outer stream or the DEX concentration in the inner stream is increased, the system becomes more susceptible to phase separation and, due to the gradient of concentration of species across the width of the channel, invasion fronts advance to regions of higher tension.

In experiments where C_{DEX_2} is kept constant and C_{PEG_1} is varied from 0 to 1 w/v%, the initial flow conditions, with fixed flow rates, can be assumed to be approximately the same since the viscosity of outer stream does not change significantly as the concentration of PEG increases. Based on measurements, the viscosity $\eta_{\mathrm{DEX\ 5w/v\%}}$ = 5 mPa s, while $\eta_{\mathrm{DEX\ 5w/v\%+PEG\ 1w/v\%}}$ = 7 mPa s. However, in experiments where C_{PEG_1} and C_{DEX_1} are kept constant, and C_{DEX_2} is varied from 5 to 30 w/v%, the initial flow profiles corresponding to each C_{DEX_2} would not be the same, since $\eta_{\mathrm{DEX\ 5w/v\%}}$ = 5 mPa s and $\eta_{\mathrm{DEX\ 30w/v\%}}$ = 151 mPa s. This effect is also evident in Fig. 3(b), where the cross sectional area that solution 2 occupies increases with increasing C_{DEX_2}.

We quantify the invasion fronts for different experiments by measuring the width of the front relative to its initial width at the junction of the microfluidic device. The data extracted from experiments in which C_{PEG_1} was varied (while keeping the DEX concentration in the inner and outer streams constant) are shown in Fig. 4(a) (see Video 2, ESI†), while experimental results in which C_{DEX_2} was varied are presented in Fig. 4(c): the rate of invasion increases as either C_{PEG_1} or C_{DEX_2} is increased. The increase of either C_{PEG_1} or C_{DEX_2} increases the free energy of the system, making it more susceptible to liquid–liquid phase separation. We can further qualitatively analyze how the final composition of the flow system varies as either C_{PEG_1} or C_{DEX_2} is varied by inspecting the binodal curve of the system, as shown in Fig. 4(b) and (d). Blue dotted lines connecting inner and outer stream compositions illustrate possible final composition of the system, which is dependent on the relative speed of the flow system and volume fraction of the two streams. As shown in Fig. 4(b) and (d), the final possible compositions tend to move towards the two-phase region as either C_{PEG_1} or C_{DEX_2} is increased.

Experimentally, for cases of C_{PEG_1} = 0 and 0.5 w/v%, we do not observe nuclei forming within the flow system. Specifically for the case of C_{PEG_1} = 0.5 w/v%, by inspecting the binodal curve in Fig. 4(b), we can see that the dotted line connecting the composition of the inner and outer stream crosses the binodal curve, however, it is possible for the final composition to remain in the one-phase regime. As C_{PEG_1} further increases, a larger portion of the possible final compositions may be in the two-phase regime.

For experiments where C_{DEX_2} is varied, we observe that based on Fig. 4(d), the final composition of the system with C_{DEX_2} = 5 and 10 w/v% always stays within the miscible regime. We further tune C_{DEX_2} within 10 w/v% to 20 w/v%, for which the results are shown on Fig. S3 and Section S3, ESI.† We find through experiments, and based on the binodal curve of the system, C_{DEX_2} >15 w/v% is needed in order to induce liquid–liquid phase separation and therefore form invasion fronts within the flow system. Otherwise, for $C_{\mathrm{DEX}_2} \leq$ 15 w/v%, the system is miscible, and no invasion fronts are formed.

Taking into account the average flow velocity of solution 1 and using data shown in Fig. 4(a) and (c), we find the fastest rate of invasion, corresponding C_{PEG_1} = 1 w/v% and C_{DEX_2} = 30 w/v%, to be $U_{\mathrm{invasion}} \approx 34\ \mu\mathrm{m\ s}^{-1}$. The slowest rate of invasion, corresponding to C_{PEG_1} = 0 w/v%, is found to be $U_{\mathrm{invasion}} \approx 4\ \mu\mathrm{m\ s}^{-1}$, while the speed corresponding to the case of C_{DEX_2} = 5 w/v% is found to be $U_{\mathrm{invasion}} \approx 2.5\ \mu\mathrm{m\ s}^{-1}$. Considering the fastest rate of invasion, corresponding to C_{PEG_1} = 1 w/v% and C_{DEX_2} = 30 w/v%, the difference in interfacial tension necessary to drive the invasion formation can be estimated as $\Delta\gamma \approx \eta_1 U_{\mathrm{inv}}$ (which can be found by equating the stress gradient and viscous dissipation in the Stokes equation), and it is found to be $\Delta\gamma \approx \mathcal{O}(10^{-7})\ \mathrm{N\ m}^{-1}$. This may be an underestimate of the interfacial tension, since due to water withdrawal from the tip of the invasion front, the real viscosity of the tip of the invasion front should be higher than η_1. However, this estimate is close to values found in the literature for such systems.[14] For systems that undergo liquid–liquid phase separation, higher gradients in polymer concentrations across the two solutions lead to a higher effective gradient in interfacial tension, resulting in a higher speed of invasion since the speed of invasion U_{invasion} is proportional to gradient in tension $\nabla\gamma$.

There are two important time scales in this system. One is the diffusion time scale of water, t_{diff} since water diffusivity $D_{\mathrm{H_2O}} \gg D_{\mathrm{PEG}} > D_{\mathrm{DEX}}$), and the other is the invasion front time scale, t_{inv}. Considering a system of DEX 30 w/v% surrounded by a miscible mixture of DEX 5 w/v% and PEG 1 w/v% (purple data series in Fig. 4(a), we find that for the front to move the half-width of the channel cross section (300 μm), the corresponding $t_{\mathrm{inv}} \approx$ 8 s. Considering the time scale of water diffusing the same length of 300 μm, we find $t_{\mathrm{diff}} \approx$ 100 s. With $t_{\mathrm{inv}} \ll t_{\mathrm{diff}}$, the system, as seen in Fig. 3(a), is controlled by the active spreading due to the dynamic liquid–liquid phase separation process.

Considering a system of DEX 30 w/v% surrounded by an outer stream of DEX 5 w/v% (Fig. 4(a) red data series), we find $t_{\mathrm{inv}} \approx$ 100 s, so $t_{\mathrm{diff}} = t_{\mathrm{inv}}$. As seen in Fig. 3(a), the Alexa dye diffuses transverse to the axial flow, without formation of invasion fronts. Without the presence of PEG within the outer stream, there is effectively no gradient in tension across the two streams. Therefore, the Alexa Fluor dye diffuses transverse to the flow, without the formation and advancement of a PEG-rich wetting front.

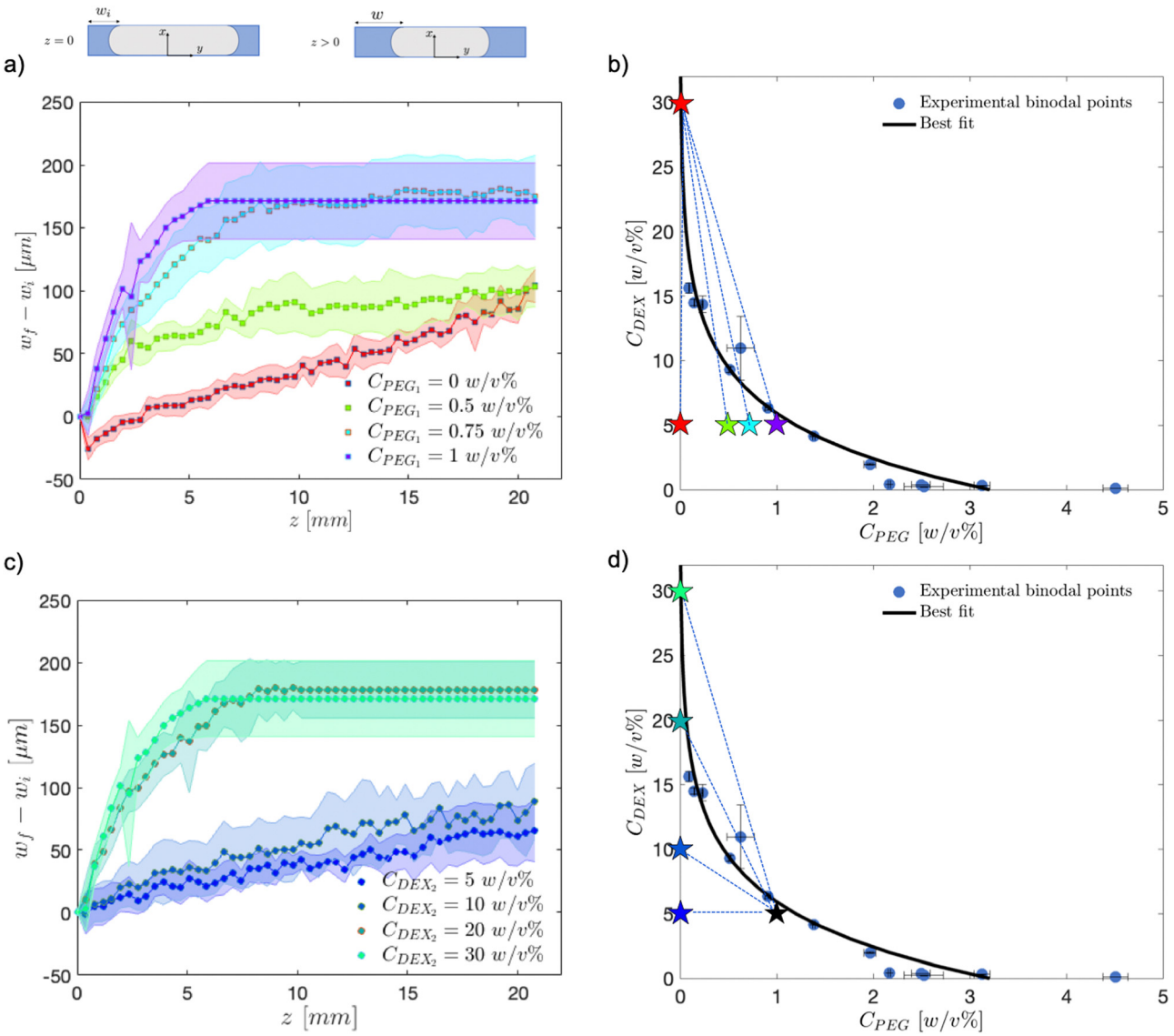

Fig. 4 (a) Plot of the relative width of the moving front, w_f, relative to the initial width of solution 1 at the junction of the device, w_i, when C_{PEG_1} is varied from 0, 0.5, 0.75 and 1 w/v% while keeping C_{DEX_1} = 5 w/v% and C_{DEX_2} = 30 w/v%. (b) Binodal curve of the ATPS with colored star markers indicating changes to C_{PEG_1} as C_{DEX_1} and C_{DEX_2} are kept constant. The blue dashed lines connecting the composition of the inner stream to the outer stream illustrate the range of possibilities for the composition of the mixture of the inner and outer streams. (c) Plot of the relative width of the moving front, w_f, relative to the initial width of solution 1 at the junction of the device, w_i, when C_{DEX_2} is varied from 5, 10, 20 and 30 w/v% while keeping C_{DEX_1} = 5 w/v% and C_{PEG_1} = 1 w/v%. (d) Binodal curve of the ATPS with colored star markers indicating changes to C_{DEX_2} as C_{PEG_1} and C_{DEX_1} are kept constant. All experiments have Q_1 = 2 μl min^{-1} and Q_2 = 1 μl min^{-1}. Increase of either C_{PEG_1} or C_{DEX_2} increases the rate of invasion of the moving fronts on both top and bottom walls. A drastic change in the slope of a data series can be seen by contrasting miscible systems to those that undergo liquid–liquid phase separation. The results shown in plots (a and c) can be further verified by assessing where the system composition is based on the binodal curve of the system. As shown in plots (b and d), the mixture composition tends to move towards the two-phase region as either C_{PEG_1} or C_{DEX_2} is increased. The shaded region in plots (a and c) correspond to standard deviation of 8 fronts (4 fronts were analyzed per experiment).

3.1.2 Changes to intensity of Alexa Fluor dye at the tip of the moving fronts with changing polymer concentration. Another facet of the observations shown on Fig. 2(b) is the change to the Alexa Fluor dye intensity at the tip of the moving front, as we view the system downstream along the length of the channel: we observe that the intensity of the fluorescent dye at the tip of the moving front increases. Since the dye has partitioning affinity to the PEG phase rather than the DEX phase (see Section S4, ESI†), we can infer that the PEG concentration in the tip of the front increases downstream along the microchannel, meaning that the front is undergoing phase separation and becoming enriched with PEG. This increase in PEG concentration is also consistent with the direction of the Marangoni flow, and the evolution of an effective interfacial

tension across the tip of the front as the system undergoes liquid–liquid phase separation.

We analyze the intensity of the dye at the tip of the front (I_{tip}) normalized by the intensity in the bulk DEX 5 w/v% + PEG 1 w/v% (I_i). As seen in Fig. 5(a), increasing C_{PEG_1} increases the rate of change of the I_{tip}/I_i. This observation is self-consistent with the fact that increasing the PEG concentration increases the susceptibility of the system to phase separate; in cases where phase separation occurs, higher initial PEG concentration results in a higher PEG concentration in the PEG-rich phase, which results in a higher dye intensity I_{tip} due to the partitioning affinity of the Alexa Fluor dye to the PEG phase. On the other hand, tuning C_{DEX_2} from 5 to 20 w/v% does not affect the intensity of the tip of the front as much, as shown in Fig. 5(b).

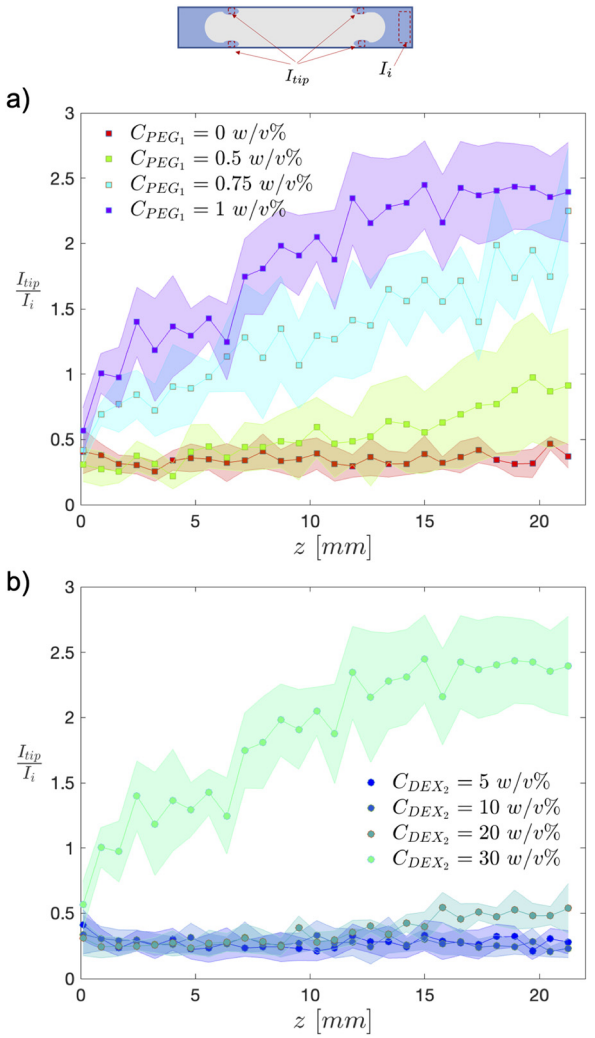

Fig. 5 Plots of normalized intensity of the Alexa Fluor dye in the moving fronts (I_{tip}) with respect to bulk outer stream intensity (I_i) *versus* position z downstream in the microchannel when (a) C_{PEG_1} and (b) C_{DEX_2} are varied. As either C_{PEG_1} or C_{DEX_2} is increased, the intensity of the fluorescent probe at the tip of the moving front increases. Given the partitioning affinity of the Alexa Fluor dye to PEG rather than DEX, and the solvent effect on the fluorescence intensity (see Section S5, ESI†), increase of I_{tip}/I_i is indicative of an increase of PEG concentration at the tip of the moving fronts, which is consistent with effective gradient in tension transporting PEG to the fronts. Moreover, it is indicative of the susceptibility of the system to phase separate.

However, a drastic change in I_{tip}/I_i is observed once C_{DEX_2} is increased from 20 to 30 w/v%. Through calibration experiments, we find that the intensity measurements are not only affected by the Alexa Fluor concentration, but also by the polymer concentration within the system (see Fig. S5, ESI†). We hypothesize that decreasing C_{DEX_2} results in a lower PEG-rich phase concentration, which inevitably results in reduced partitioning of Alexa Fluor dye into the PEG-rich phase. Moreover, considering systems that have fully phase separated, we find from bulk experiments that $I/I_i \approx 3.3$ for a PEG-rich phase from ATPS of DEX 30 w/v% and DEX 5 w/v% and PEG 1 w/v%, while $I/I_i \approx 1.3$ for a PEG-rich phase from ATPS of DEX 20 w/v% and DEX 5 w/v% and PEG 1 w/v%, which further confirms that the changes in I/I_i with z for a flow system with inner stream of DEX 20 w/v% are expected to be lower compared to flow system with inner stream of DEX 30 w/v%.

3.2 Transient flow system

It takes about 30 minutes for the flow system to reach steady-state, after which there are no further changes in the cross section of the flow. But how is steady-state established for these systems? To address this question, we observe the evolution of the flow in the cross section, from the time that solution 2 is injected into the system, at four different positions (z = 0 mm, z = 3 mm, z = 6 mm, and z = 9 mm), as shown in Fig. 6(a) and Video 3, ESI.† Due to limitation of the confocal microscopy at higher scanning frequencies, we are only able to visualize 400 μm of the 600 μm wide channel.

As the inner stream, DEX 30 w/v%, is injected into the microchannel, the intensity of the Alexa Fluor dye in the center of the channel decreases. However, after sometime, as the inner stream pushes the outer stream towards the wall (with some mixing happening locally near the center of the channel) regions of high intensity Alexa Fluor dye appear near the center line of the channel z = 0, 3, 6, and 9 mm, as seen in Fig. 6(a). Due to the affinity partitioning of the dye to the PEG phase, we infer that the high intensity Alexa Fluor dye region that appears should be a PEG-rich zone. At z = 3 and 6 mm cross sections, we observe that this PEG-rich zone becomes unstable, thinning and losing intensity with time, and, in the end, the PEG-rich zone splits into segments (only the right-hand side segment can be seen in Fig. 6(a). However at z = 9 mm, the PEG-rich zone does not become unstable, it stays intact, with a noticeably higher dye intensity within the PEG-rich zone at this cross section compared to positions further upstream (see Video 3, ESI,† which shows how the system at each position z reaches steady-state).

We quantify the intensity of the Alexa Fluor dye in a fixed regions of interest, centered along the center line of the channel (I_{ROI}) as shown in the inset of Fig. 6(b), normalized by the intensity within the bulk DEX 5 w/v% and PEG 1 w/v% solution (I_i) (see Section S6, ESI†), for different z positions. We observe that at about t = 2 min the intensity drops to 0 and subsequently increases. This increase corresponds to formation

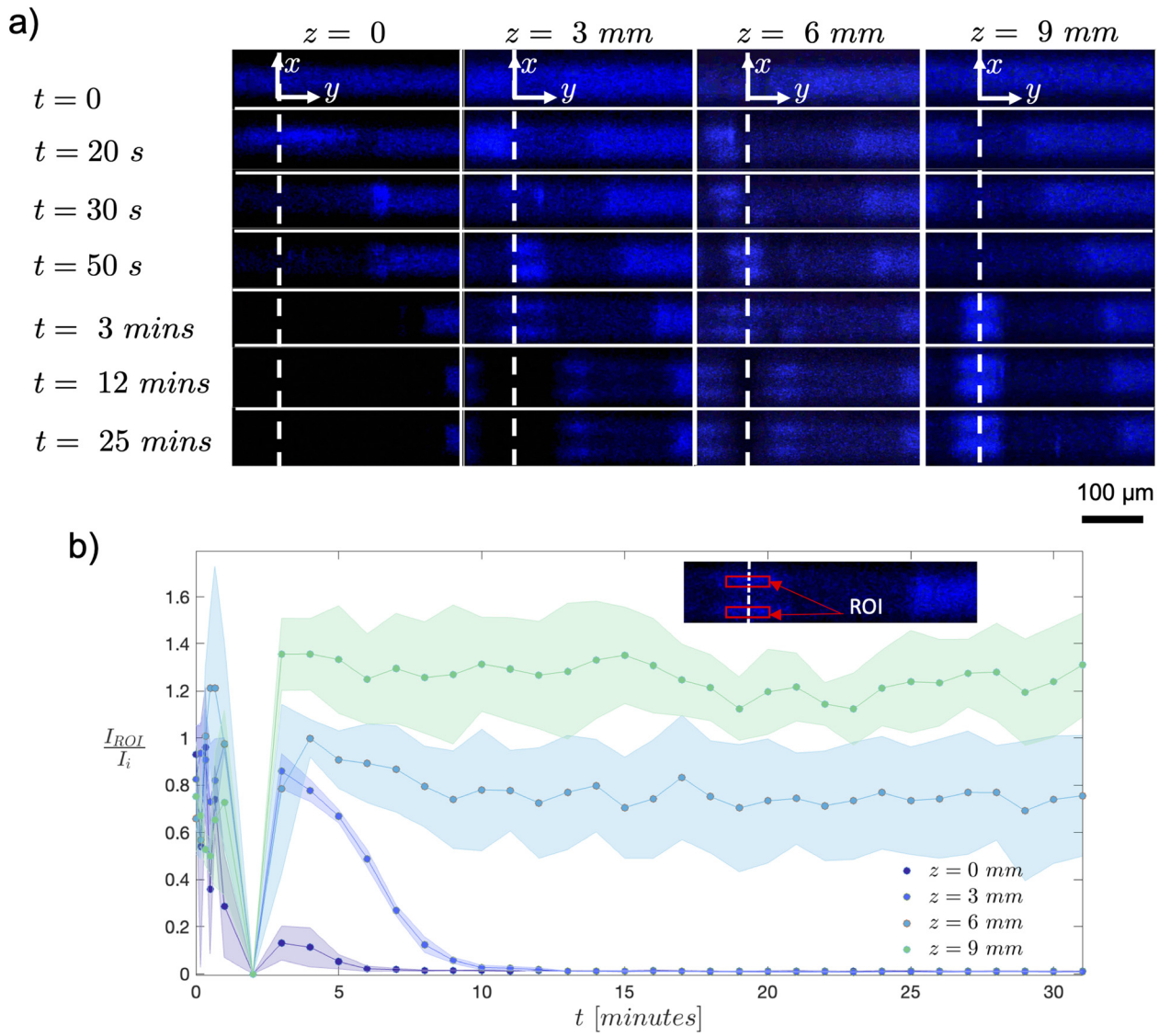

Fig. 6 (a) Temporal images of the cross section of the flow system, at different positions. First the channel is filled with miscible solution of DEX 5 w/v% and PEG 1 w/v%. Then at t = 0, the inner stream of DEX 30 w/v% is flowed into the microchannel. As the inner stream displaces the outer stream, PEG-rich droplets zones nucleate on the top and bottom wall close to the center of the microchannel. However, with time, at positions z = 3 and 6 mm, the Alexa Fluor dye intensity within the droplet decreases with time, and at about t = 12 min, the droplet splits into two, forming the tips of the outer stream fronts of the steady-state configuration. Further downstream, at z = 9 mm, the PEG-rich zones that had formed remain. White dashed lines illustrate the center line of the channel. (b) Normalized intensity of region of interest I_{ROI}/I_i *versus* time t, at different positions z. After the inner stream displaces the miscible solutions of DEX 5 w/v% and PEG 1 w/v%, and a PEG-rich droplet is nucleated, the intensity of the Alexa Fluor dye within the region of interest decays at z = 0 and 3 mm, while it remains constant at z = 6 and 9 mm.

of the PEG-rich zone near the center at the different cross sections near the center line. With time, the intensity of the PEG-rich zone at positions z = 0, 3 mm decays to 0, while for positions z = 6, 9 mm, the intensities plateau (with the normalized intensity being roughly 40% higher for z = 9 mm compared to z = 6 mm). The decay of signals at positions z = 0, 3 mm indicates the split of the PEG-rich zones, and formation of the final three-dimensional flow configuration.

The reason for decaying I_{ROI}/I_i, and the split and recession of PEG zone at positions z = 0 and 3 mm over long times, from the center of the channel towards the wall is due to the composition of the PEG zone at the different positions. Based on Fig. 6(b), we observe that the peak I_{ROI}/I_i for the four data series after t = 2 min increases with distance downstream, z. Furthermore, it is known that the normalized intensity of the dye within these immiscible systems increases with the concentration of the phase-separated PEG. Given that the peak I_{ROI}/I_i at positions z = 0 and 3 mm is lower than at positions z = 6 and 9 mm, we can conclude that the concentration of PEG in the PEG-rich zone at positions z = 0 and 3 mm is lower than positions downstream. Since the PEG-rich zones are not stable, we can conclude that the concentration of PEG in the PEG-rich zone, and the surrounding DEX at positions z = 0 and 3 is within the miscible regime of the binodal curve. Therefore, the

tension is not strong enough to keep the PEG-rich zone near the center line intact. Hence, the PEG-rich zone becomes unstable and splits into two, and in time, the split segments recede towards the side walls of the device, resulting in a final configuration of the invasion fronts we observed when the system reaches steady-state.

4 Conclusions

In this work, we show how co-flow of nonequilibrated aqueous flows can lead to the formation of invasion fronts once the system has reached steady-state, facilitated by the preferential wettability of the nucleated phase to the walls of the channel. By tuning the concentration of polymers within these systems, we show that higher polymer concentrations result in a faster evolution of the dynamic wetting fronts. The formation of these wall-wetting invasion fronts are consistent with Marangoni flow in that the strong composition gradient transverse to the flow downstream can lead to formation and advancement of fronts towards regions of higher tension. In the end, we show how the system reaches steady-state at different positions along the length of the channel.

Nonequilibrated all-aqueous systems are rich platforms that allow for microdroplet formation and transport of species. Based on the results from our study, the species present within the system and their respective wettability to the surface of the channel may affect the flow evolution in the microchannels, which would have a strong impact on the transport of materials. Therefore, no matter what type of application these nonequilibrated systems are designed for, it is important to think about how phase separation and enrichment of different phases within the process affect the flow outcome, and perhaps whether surface treatment may be desired to either prevent or promote heterogeneous nucleation.

There are many parameters within this study that are yet to be explored. For instance, based on interfacial tension measurements, how do the invasion speeds from flow experiments compare with typical speeds estimated by gradients in tension? How does the relative speed of one phase to another, coupled with preferential wettability of each phase to the walls, affect the phase separation process and inevitability the flow profile along the length of the channel? How do changes in speed affect the liquid–liquid phase separation process, *i.e.*, are there specific background flow regimes for heterogeneous *versus* homogeneous nucleation? Specifically for studies on understanding the role of downstream advection, either tuning the flow rate ratio between the two streams (while keeping one stream's flow rate fixed), or tuning the total flow rate within the system (while keeping the flow rate ratio fixed), can provide more insight on the evolution of such nonequilibrated flows and the coupling between hydrodynamics and the liquid–liquid phase separation process. These and many more questions motivate further study for better understanding and designing these all-aqueous flow platforms for various biotechnological applications.

Author contributions

N. A., J. K. N. and H. A. S. conceptualized the research. N. A. and J. K. N. designed the methodology. N. A. performed the experiments and analyzed the data. N. A., J. K. N., Z. P., T. D., H. C. S., A. K. and H. A. S. contributed to data interpretation and discussion. N. A., J. K. N. and H. A. S. wrote the original draft of the paper, and Z. P., T. D., H. C. S., and A. K. contributed to review and editing.

Conflicts of interest

There are no conflicts to declare.

Acknowledgements

H. A. S., A. K., J. K. N., T. D., and N. A. acknowledge support from National Science Foundation (NSF) through the Princeton University (PCCM) Materials Research Science and Engineering Center DMR-2011750 and Hong Kong RGC Research Impact Fund No. R7072-18. N. A. is grateful for support from Natural Sciences and Engineering Research Council of Canada (NSERC) Postgraduate Scholarship Doctoral (PGS D) Program. The authors acknowledge the use of the Micro/Nanofabrication Center at the Princeton Materials Institute, and the scientific support staff members who made these studies possible.

Notes and references

1 Y. Xia and G. M. Whitesides, *Annu. Rev. Mater. Sci.*, 1998, **28**, 153–184.
2 P.-A. Albertsson, *Nature*, 1956, **177**, 771–774.
3 E. Eriksson, P. k Albertsson and G. Johansson, *Mol. Cell. Biochem.*, 1976, **10**, 123–128.
4 B. A. Andrews, A. S. Schmidt and J. A. Asenjo, *Biotechnol. Bioeng.*, 2005, **90**, 380–390.
5 S. Hardt and T. Hahn, *Lab Chip*, 2012, **12**, 434–442.
6 Y. Chao and H. C. Shum, *Chem. Soc. Rev.*, 2020, **49**, 114–142.
7 H. C. Shum, J. Varnell and D. A. Weitz, *Biomicrofluidics*, 2012, **6**, 012808.
8 B. Moon, S. G. Jones, D. K. Hwang and S. S. Tsai, *Lab Chip*, 2015, **15**, 2437–2444.
9 B.-U. Moon, N. Abbasi, S. G. Jones, D. K. Hwang and S. S. H. Tsai, *Anal. Chem.*, 2016, **88**, 3982–3989.
10 M. Jeyhani, R. Thevakumaran, N. Abbasi, D. K. Hwang and S. S. H. Tsai, *Small*, 2020, **16**, 1–10.
11 K. Zhu, Y. Yu, Y. Cheng, C. Tian, G. Zhao and Y. Zhao, *ACS Appl. Mater. Interfaces*, 2019, **11**, 4826–4832.
12 M. S. Long, C. D. Jones, M. R. Helfrich, L. K. Mangeney-Slavin and C. D. Keating, *Proc. Natl. Acad. Sci. U. S. A.*, 2005, **102**, 5920–5925.
13 S. D. Hann, K. J. Stebe and D. Lee, *Langmuir*, 2017, **33**, 10107–10117.
14 E. Atefi, J. A. Mann and H. Tavana, *Langmuir*, 2014, **30**, 9691–9699.

15 S. D. Geschiere, I. Ziemecka, V. van Steijn, G. J. M. Koper, J. H. van Esch and M. T. Kreutzer, *Biomicrofluidics*, 2012, **6**, 022007.
16 Y. Chao, S. Y. Mak, S. Rahman, S. Zhu and H. C. Shum, *Small*, 2018, **14**, 1–7.
17 Y. Chao, L. T. Hung, J. Feng, H. Yuan, Y. Pan, W. Guo, Y. Zhang and H. C. Shum, *Soft Matter*, 2020, **16**, 6050–6055.
18 Y. Chao, S. Y. Mak, Q. Ma, J. Wu, Z. Ding, L. Xu and H. C. Shum, *Langmuir*, 2018, **34**, 3030–3036.
19 N. Abbasi, M. Navi, J. K. Nunes and S. S. H. Tsai, *Soft Matter*, 2019, **15**, 3301–3306.
20 B.-U. Moon, D. K. Hwang and S. S. H. Tsai, *Lab Chip*, 2016, **16**, 2601–2608.
21 H. Tan, C. Diddens, P. Lv, J. G. M. Kuerten, X. Zhang and D. Lohse, *Proc. Natl. Acad. Sci. U. S. A.*, 2016, **113**, 8642–8647.
22 B.-U. Moon, L. Malic, K. Morton, M. Jeyhani, A. Elmanzalawy, S. S. H. Tsai and T. Veres, *Langmuir*, 2020, **36**, 14333–14341.
23 A. May, J. Hartmann and S. Hardt, *Soft Matter*, 2022, **18**, 6313–6317.
24 P. G. Moerman, P. C. Hohenberg, E. Vanden-Eijnden and J. Brujic, *Proc. Natl. Acad. Sci. U. S. A.*, 2018, **115**, 3599–3604.
25 M. A. Khan, A. J. Sprockel, K. A. Macmillan, M. T. Alting, S. P. Kharal, S. Boakye-Ansah and M. F. Haase, *Adv. Mater.*, 2022, **34**, 2109547.
26 M. F. Haase and J. Brujic, *Angew. Chem.*, 2014, **126**, 11987–11991.
27 R. Hajian and S. Hardt, *Microfluid. Nanofluid.*, 2015, **19**, 1281–1296.
28 M. F. Haase, K. J. Stebe and D. Lee, *Adv. Mater.*, 2015, **27**, 7065–7071.
29 X. Zhang, J. B. You, G. F. Arends, J. Qian, Y. Chen, D. Lohse and J. M. Shaw, *Soft Matter*, 2021, **17**, 5362–5374.
30 G. F. Arends, J. M. Shaw and X. Zhang, *Energy Fuels*, 2021, **35**, 11257–11270.
31 T. Zinn, L. Sharpnack and T. Narayanan, *Phys. Rev. Res.*, 2020, **2**, 033177.
32 A. G. L. Williams, G. Karapetsas, D. Mamalis, K. Sefiane, O. K. Matar and P. Valluri, *J. Fluid Mech.*, 2021, **907**, A22.
33 Y. Chao, O. Ramírez-Soto, C. Bahr and S. Karpitschka, *Proc. Natl. Acad. Sci. U. S. A.*, 2022, **119**, e2203510119.
34 A. T. Rowland and C. D. Keating, *Soft Matter*, 2021, **17**, 3688–3699.
35 D. T. Eddington, J. P. Puccinelli and D. J. Beebe, *Sens. Actuators, B*, 2006, **114**, 170–172.
36 J. Schindelin, I. Arganda-Carreras, E. Frise, V. Kaynig, M. Longair, T. Pietzsch, S. Preibisch, C. Rueden, S. Saalfeld, B. Schmid, J.-Y. Tinevez, D. J. White, V. Hartenstein, K. Eliceiri, P. Tomancak and A. Cardona, *Nat. Methods*, 2012, **9**, 676–682.
37 M. Tsukamoto, S. Taira, S. Yamamura, Y. Morita, N. Nagatani, Y. Takamura and E. Tamiya, *Analyst*, 2009, **134**, 1994–1998.
38 Y. Liu, R. Lipowsky and R. Dimova, *Langmuir*, 2012, **28**, 3831–3839.